Fracture Detection using Amplitude versus Offset and Azimuth Analysis of a 3D P-wave Seismic Dataset and Synthetic Examples

Burke J. Minsley, Mark E. Willis, Mary Krasovec, Daniel R. Burns, and M. Nafi Toksöz
Earth Resources Laboratory
Dept. of Earth, Atmospheric, and Planetary Sciences
Massachusetts Institute of Technology
Cambridge, MA 02139

26 May 2004

Abstract

Amplitude versus offset (AVO) analysis of seismic reflection data has been a successful tool in describing changes in rock properties along a reflector. This method is extended to azimuthal AVO (AVOA) in order to characterize vertically aligned fractures within a reservoir, which can be important fluid migration pathways. AVOA analysis is performed on synthetic data using a least squares inversion method to investigate the effects of varying acquisition geometry, amount of noise, and fracture properties. These tests show that it is possible to detect the fractured layer and determine the fracture strike orientation under typical acquisition conditions. This method is also applied to field data collected during an Ocean Bottom Cable (OBC) survey. These data include a broad offset-azimuth range, which is important for the AVOA analysis. The fracture location and strike orientation recovered from the field data analysis are well correlated with borehole information from this area. Based on an understanding of AVOA behavior under synthetic conditions, this technique provides an effective methodology for describing the spatial variability of a fractured reservoir using 3D seismic data.

1 Introduction

1.1 Objectives

Open fractures can have a significant impact on the flow of fluids within a reservoir, especially if they are interconnected over large distances. Fractures are often oriented in preferential directions determined by regional stresses and the geologic structures in which they reside (Walsh and Brace, 1964). Improved recovery of reservoir fluids can be realized by drilling production wells normal to the fracture strike direction, thereby maximizing the capture area of the well. Successful implementation of this technique relies on the ability to describe the location, orientation, and fluid content of fractures over a large area with good spatial resolution. Although fracture information can be found directly from various well-logging techniques, this is not an effective way to describe spatial changes in fracture properties throughout a large reservoir. This study is focused on the use of 3D seismic reflection data to provide spatially continuous information about aligned vertical fractures.

Amplitude versus offset (AVO) analysis has proven useful in characterizing changes in material properties along a reflector. In the case of a fractured reservoir the AVO behavior varies with fracture density, aspect ratio, and saturating fluid. The introduction of fractures or changes in their properties throughout a reservoir will be visible as an AVO anomaly. For vertically aligned fractures that are of interest in this study there will also be an azimuthal dependence of the AVO response that is related to the fracture strike orientation. Extension to azimuthal AVO (AVOA) is therefore appropriate because it allows for the simultaneous analysis of seismic data collected at different azimuths relative to the fractures.

Surveys that include a wide range of offsets and azimuths have become more common and are ideally suited to AVOA studies. The promise of using AVO as a reconnaissance/analysis tool with regard to fracture properties is quite attractive because it is a relatively inexpensive addition to the typical acquisition and processing of seismic

data. In this study, least squares methods are developed to quantify the utility of P-wave AVOA analysis on synthetic data. These results help to guide the analysis of a 3D OBC dataset collected over the fractured Emilio Field located in the Adriatic Sea.

1.2 Background

The effect of many low aspect ratio fractures aligned at a preferred orientation results in seismic anisotropy. When the fracture spacing is much smaller than the seismic wavelengths of interest, the material is often expressed as an effective medium. For vertically oriented fractures the medium is transversely isotropic with a horizontal axis of symmetry (HTI), illustrated in Figure 1. The effective elastic moduli at different orientations with respect to the fractures are controlled by different compliances in these directions (Schoenberg, 1995) and result in the observed seismic azimuthal anisotropy.

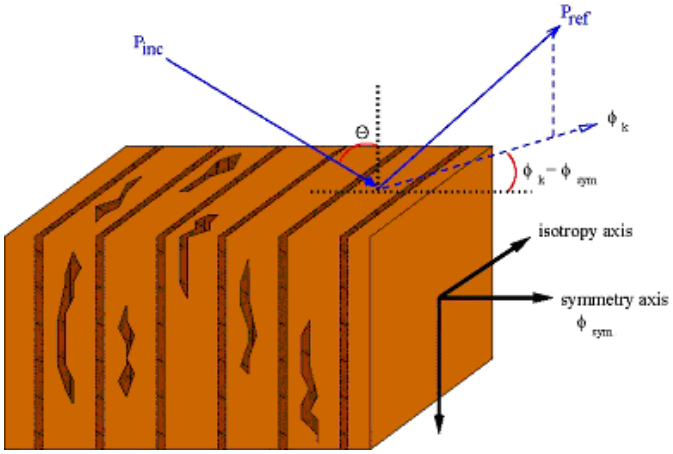

Figure 1: Cartoon of HTI model with vertically aligned fractures

The underlying concept behind AVO was developed by Knott and Zoeppritz near the beginning of the 20th century. By imposing conditions of continuous stress and displacement at the interface between two materials, they give relationships for the amplitudes of reflected and transmitted P and S waves as a function of incidence angle. These relationships are complicated functions of V_P, V_S, and ρ for the two media, and are put into a useful matrix form by Aki and Richards (1980). Simplifications of the general Zoeppritz equations have since been made that are applicable to the relatively subtle changes found in Earth materials at angles of incidence commonly used in exploration seismology. Shuey (1985) presents a simplified form for the reflected P-wave amplitudes as a function of incidence angle that provides the basis for the AVO model in this study. An extension of the Shuey method that describes AVOA for the HTI case was made by Rüger (1997).

There are many examples of techniques used for measuring the response of HTI media using AVO and AVOA (Lynn *et. al.*, 1996; Mallick *et. al.*, 1998; Shen *et. al,* 2002; Hall and Kendall, 2003), as well velocity oriented methods such as shear-wave birefringence (Gaiser *et. al.*, 2002; Vetri *et. al.*, 2003). A recent work by Dong and Davidson (2003) addresses the issue of 3D survey geometry and it implications for the adequacy of AVOA analysis. While much work is based on theoretical models, there is also a large amount of AVO analysis performed on field data, particularly in the exploration industry.

1.3 Methodology

A simple two-layer model is studied in order to understand the estimates and assumptions commonly made with least squares inversion methods applied to AVO analysis. The effects of these estimations, as well as geometry and noise considerations, are taken into account. The synthetic model is then extended to an HTI regime and similar analysis methods are developed for the azimuthally varying Rüger approximation. This is accomplished with a surface-fitting algorithm for the AVOA analysis that is similar to the approach of Hall and Kendall (2003). Many other azimuthal AVO studies separate the data into a few discrete azimuths and compare the individual AVO results

in those directions. The strength of this investigation lies in the analysis of a full range of azimuths simultaneously, better constraining the problem.

Data acquired during a 3D OBC survey are inverted for azimuthal AVO parameters using the techniques developed here. Inference from the behavior of the synthetic tests helps guide the interpretation of the OBC results and direct future improvements. In addition, results of the AVOA analysis on a synthetic dataset created with a 3D finite difference forward modeling code and fractured model is given in Appendix A.

2 Development

2.1 AVO Approximation

It is useful to begin with a description of Shuey's approximation of the Zoeppritz equations. For an interface between two layers with P-wave velocities V_{P1} and V_{P2}, densities ρ_1 and ρ_2, and Poisson's ratios σ_1 and σ_2, the angle of incidence-dependent reflectivity, $R_{PP}(\Theta)$, is given by Castagna (1993) as

$$R_{PP}(\Theta) \approx R_P + \left[A_0 R_P + \frac{\Delta\sigma}{(1-\sigma)^2}\right]\sin^2\Theta + \frac{1}{2}\frac{\Delta V_P}{V_P}\left(\tan^2\Theta - \sin^2\Theta\right) \tag{1}$$

where,

$$R_P = \frac{\rho_2 V_{P2} - \rho_1 V_{P1}}{\rho_2 V_{P2} + \rho_1 V_{P1}} \tag{2}$$

$$A_0 = B_0 - 2(1+B_0)\frac{(1-2\sigma)}{(1-\sigma)} \tag{3}$$

$$B_0 = \frac{\frac{\Delta V_P}{V_P}}{\frac{\Delta V_P}{V_P} + \frac{\Delta\rho}{\rho}} \tag{4}$$

and,

$$\begin{aligned} \sigma &= \frac{\sigma_2 + \sigma_1}{2}, \qquad \Delta\sigma = \sigma_2 - \sigma_1 \\ V_P &= \frac{V_{P2} + V_{P1}}{2}, \quad \Delta V_P = V_{P2} - V_{P1} \\ \rho &= \frac{\rho_2 + \rho_1}{2}, \qquad \Delta\rho = \rho_2 - \rho_1 \end{aligned} \tag{5}$$

Equation (1) can be written as a linear equation in three parts, commonly given in terms of AVO coefficients A, B, and C.

$$R_{PP} \approx A + B\sin^2\Theta + C\left(\tan^2\Theta - \sin^2\Theta\right) \tag{6}$$

The 'A' term, equal to R_P, describes the normal incidence ($\Theta = 0$) reflectivity, while the $\sin^2$ term applies to angles of incidence up to about 30 degrees, and the ($\tan^2 - \sin^2$) term dominates for angles mostly above 30 degrees. This last term is sometimes disregarded in AVO analysis because angles of incidence are larger than those used in most exploration surveys.

Each term in Equation (6) involves a combination of elastic constants, a fact that limits the ability to classify material changes through AVO model parameters alone. Also, note that R_{PP} represents the actual value of the reflection coefficient given in Equation (1). This is a difficult quantity to obtain with reflection seismic data, and actual reflection amplitudes are often used instead because they are proportional to the reflection coefficient. This approximation further degrades the ability to use AVO as a quantification tool with regards to material properties.

2.2 Extension to AVOA in HTI Media

Equation (6) describes the reflection amplitude dependence as a function of offset (or angle of incidence) and elastic constants for two isotropic media. For the HTI model (Figure 1), a set of vertically aligned fractures embedded in a homogeneous background material is used. These fractures typically have small aspect rations due to the orientation of local stresses. In the direction of the isotropy axis, these apparently thin fractures have little effect

on the elastic properties, and thus reflection amplitudes, compared with the homogeneous case. For ray-paths along the symmetry-axis however, fracture compliance plays a significant role in the behavior of reflection amplitudes. This is a manifestation of the rock and fluid compressibility, density, and fracture geometry. These two directions represent the extremes of the azimuthal AVO behavior, and seismic waves typically propagate more slowly in the fracture normal (symmetry-axis) direction.

An analysis of seismic waves propagating over a 180 degree range of azimuths should therefore sample one complete 'cycle' of the transverse isotropy. The goal of AVOA analysis is to capture the azimuthal variation of reflection amplitudes, which requires data collected at an absolute minimum of three independent azimuths. In practice, wide-azimuth 3D survey methods are required to adequately sample the offset-azimuth space. Reflection amplitudes at a given offset will have an azimuthal dependence that is periodic with respect to the symmetry axis.

Rüger's addition to Shuey's approximation captures this azimuthal variation in amplitudes. The AVO gradient ('B') term is split into a constant, isotropic term, and an azimuthally varying anisotropic term.

$$B(\varphi_k) = B^{iso} + B^{ani}\cos^2(\varphi_k - \varphi_{sym}) \tag{7}$$

In this equation, φ_k represents an arbitrary source to receiver azimuth within the dataset, and φ_{sym} represents the unknown symmetry-axis orientation. This is a non-linear equation with several terms coupled together. The result of this non-linearity is that there are two combinations of B^{iso}, B^{ani}, and φ_{sym} that describe the behavior of $B(\varphi_k)$ equally. These solutions will have values of φ_{sym} that are 90 degrees apart. B^{iso} and B^{ani} will both have the same sign for one solution and opposite signs and different values for the other. These correspond to maximum AVO behavior along the fracture symmetry axis and maximum behavior along the isotropy axis, respectively. Often, *a-priori* knowledge about the general fracture orientation or expected AVO behavior can be used to select one of the solutions. An illustration of the non-uniqueness in this problem is given in Figure 2 for a particular set of 'true' values of B^{iso}, B^{ani}, and φ_{sym} in Equation (7). The RMS error is displayed as a function of these parameters over a range of possible values.

Although there is also an azimuthal variation of the larger incidence angle 'C' term, it is not developed here due to the focus on near to intermediate angles of incidence. Equation 5 can then be written for the azimuthally varying case as

$$R_{PP} \approx A + \left[B^{iso} + B^{ani}\cos^2\left(\varphi_k - \varphi_{sym}\right)\right]\sin^2\Theta \tag{8}$$

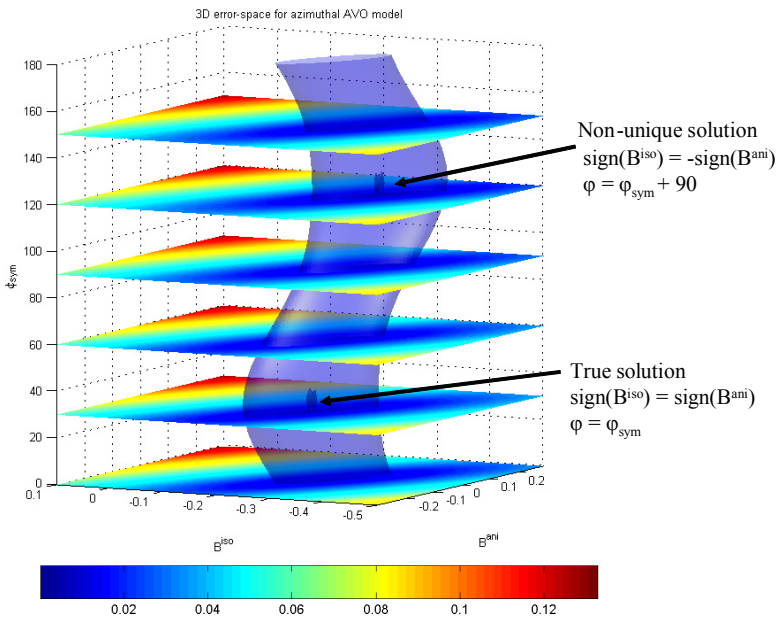

Figure 2: RMS error for the AVOA case as a function of B^{iso}, B^{ani}, and φ_{sym} with respect to a particular 'true' solution. The non-unique solution appears 90° from the true solution with different values for B^{iso} and B^{ani}.

2.3 Application of Least Squares to AVO and AVOA

2.3.1 Non-azimuthal AVO

Equation (6), the reflection amplitude behavior for non-azimuthal AVO, is a linear equation in terms of $\sin^2\Theta$ and $\tan^2\Theta$. An ordinary least squares inversion can be used in this case, where the relationship is put into a simple linear form,

$$\mathbf{E}\tilde{\mathbf{x}} + \mathbf{n} = \mathbf{y} \tag{9}$$

The solution for the over-determined problem that minimizes the data residual norm, $\|\mathbf{n}\|^2$ is

$$\tilde{\mathbf{x}} = \left(\mathbf{E}^T\mathbf{E}\right)^{-1}\mathbf{E}^T\mathbf{y} \tag{10}$$

For these linear equations, $\mathbf{y}$ represents the reflection amplitude data, $\tilde{\mathbf{x}}$ is the estimate of the AVO model parameters (A, B, and C), $\mathbf{n}$ is the data residual, and the matrix $\mathbf{E}$ (shown below) is made up of the terms including the independent variable, Θ.

$$\mathbf{E}_{AVO} = \begin{bmatrix} 1 & \sin^2\Theta & \left(\tan^2\Theta - \sin^2\Theta\right) \\ 1 & \sin^2\Theta & \left(\tan^2\Theta - \sin^2\Theta\right) \\ 1 & \sin^2\Theta & \left(\tan^2\Theta - \sin^2\Theta\right) \\ . & . & . \\ . & . & . \\ 1 & \sin^2\Theta & \left(\tan^2\Theta - \sin^2\Theta\right) \end{bmatrix} \tag{11}$$

The AVO inversion is performed on a single common mid-point (CMP) gather at a time, where each row represents a single trace in the gather and an associated incidence angle Θ.

2.3.2 Azimuthal AVO

For the case of azimuthal AVO, this ordinary least squares routine is not appropriate due to the non-linearity of Equation (8). Instead, an iterative, non-linear least squares inversion that uses the Gauss-Newton method is employed. This involves the calculation of the Jacobian matrix, $\mathbf{A}_i = \partial\mathbf{M}_i / \partial\tilde{\mathbf{x}}_i$, at each iteration. $\mathbf{M}$ is the reflectivity model for R_{PP} given by Equation (8) and $\tilde{\mathbf{x}}_i$ represents the four AVOA model variables A, B^{iso}, B^{ani}, and φ_{sym}. Starting with an initial guess for the four unknown parameters, model updates are made according to Equation (12).

$$\begin{aligned} d\tilde{\mathbf{x}}_i &= \left(\mathbf{A}_i^{\,T}\mathbf{A}_i\right)^{-1}\mathbf{A}_i^{\,T}(\mathbf{y} - \mathbf{M}_i) \\ \tilde{\mathbf{x}}_{i+1} &= \tilde{\mathbf{x}}_i + d\tilde{\mathbf{x}}_i \end{aligned} \tag{12}$$

The data vector, $\mathbf{y}$, is the same reflection amplitude data for each trace in a CMP used in the regular AVO case. At each step the solution vector $\tilde{\mathbf{x}}$ is updated and the RMS error is calculated between the measurements, $\mathbf{y}$, and the current model $\mathbf{M}_i$. When the error becomes sufficiently small, the solution has converged to $\tilde{\mathbf{x}}_i$.

Another way to solve the non-linear problem is to linearize Equation (8) so that it can be solved in one step using the ordinary least squares method of Equation (10). Using trigonometric identities for $\cos^2\left(\varphi_k - \varphi_{sym}\right)$, Equation (8) becomes

$$R_{PP} \approx A + \left(B^{iso} + \frac{1}{2}B^{ani}\right)\sin^2\Theta + \left(\frac{1}{2}B^{ani}\cos 2\varphi_{sym}\right)\cos 2\varphi_k \sin^2\Theta + \left(\frac{1}{2}B^{ani}\sin 2\varphi_{sym}\right)\sin 2\varphi_k \sin^2\Theta \tag{13}$$

and can be written as a linear equation in four unknowns

$$R_{PP} \approx C_1 + C_2\sin^2\Theta + C_3\cos 2\varphi_k \sin^2\Theta + C_4\sin 2\varphi_k \sin^2\Theta \tag{14}$$

This is similar to the approach used by Xu and Li (2001), where

$$
\begin{aligned}
A &= C_1 \\
B^{ani} &= \pm 2\sqrt{C_3^{\,2} + C_4^{\,2}} \\
B^{iso} &= C_2 - \frac{1}{2} B^{ani} \\
\varphi_{sym} &= \frac{1}{2} \arctan \frac{C_4}{C_3}
\end{aligned}
\tag{15}
$$

As with the nonlinear method, the solution is non-unique with two possible solutions corresponding to values for φ_{sym} that are 90 degrees apart. Although this is not as robust as the non-linear routine mentioned above, it is easier to employ for some of the basic synthetic examples in this study and yields identical results.

3 Synthetic Analysis

3.1 Ordinary (non-azimuthal) AVO

3.1.1 Description of the Model and Data

In order to understand the behavior of the least squares analysis, a simple model for the interface between two layers with different elastic parameters is used to create AVO coefficients based on Equation (6). This example uses the parameters summarized in Table 1 and the synthetic AVO coefficients are calculated directly from Equations (2) -(4).

	Layer 1	**Layer 2**
V_P	3000 m/s	4000 m/s
V_S	1732 m/s	2309 m/s
P	2300 kg/m^3	2600 kg/m^3
σ	0.25	0.25
AVO-A	0.202	
AVO-B	-0.316	
AVO-C	0.143	

Table 1: Elastic parameters for two-layer model

From these coefficients synthetic reflectivity data (R_{PP}) is calculated over a range of incidence angles commonly found in reflection seismology. The synthetic data is then contaminated with noise or partially removed over certain offset ranges and the ability of the inversion to recover the original coefficients is studied. The modeled behavior for the offset dependent reflectivity is shown in Figure 2, where the angles are based on fixed source-to-receiver offsets and a depth to the interface of 800m.

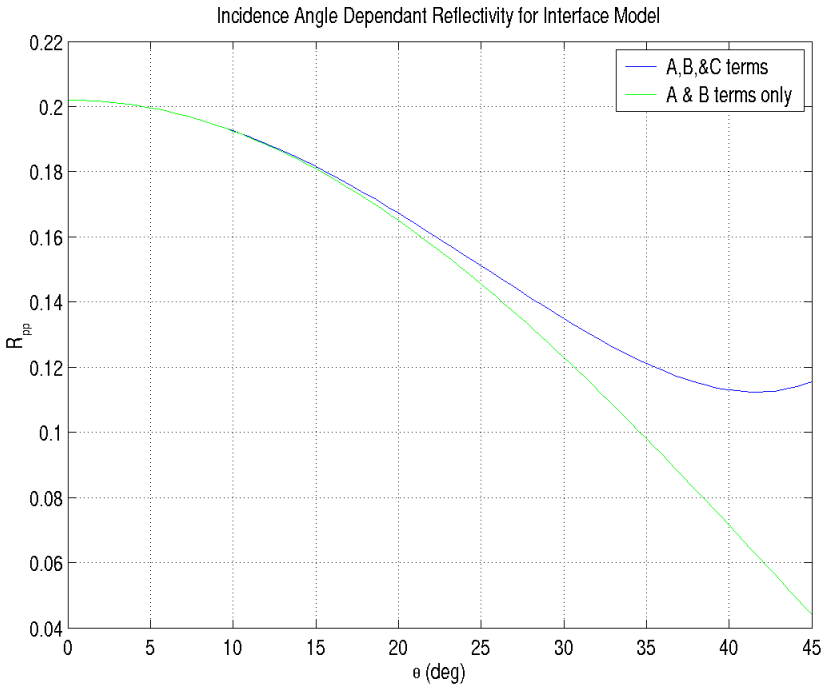

Figure 3: Modeled AVO for a simple two-layer interface using Equation (6) and the parameters in Table 1.

In this figure, the effect of modeling only the A and B terms is clear; there is little deviation below 20°, around 10% at 30°, and then they diverge significantly at larger angles. The three-term reflectivity curve will be treated as the 'true' value for the discussion of the following inversion results. The effects of changing source-to-receiver geometry are studied using both 2- and 3-term AVO models, as well as their behavior in the presence of noise. For this experiment, random noise with a Gaussian distribution and standard deviation of 0.02 is added to the 'true' reflectivity data. This standard deviation corresponds to about 13% of the mean value of the original model.

3.1.2 Synthetic AVO Tests

The first case shown in Figure 4 uses data sampled from the 'true' reflectivity curve on one degree intervals from 0° to 45°. Using the high angle of incidence data, it is clear that a 2-term AVO model is incapable of recovering the correct values, even for the noise-free case. The fact that the 2-term model is inappropriate can also be seen in the residual, which shows structure. In the presence of noise the AVO gradient term has an error of 31% for the 2-term model compared with only 8% for the 3-term model.

Typically, the source-to-receiver offsets and target depths in a seismic survey do not result in angles of incidence that extend to 45°. This experiment is therefore repeated using only data from 0° to 30°, and the results are shown in Figure 5. With noise-free data, the 2-term AVO model is more accurate than before, but is still unable to recover the true solution. When some noise is added to the reflectivity measurements, however, the 2-term and 3-term solutions become much less accurate. Repeating this experiment many times with different noise realizations, one finds that the estimate of the 3-term model is unbiased about the correct solution, but has a relatively large variance around the mean. The 2-term model estimate does not have the correct mean, but has much smaller variance.

Finally, for a more representative approximation of real acquisition geometries, information about the near offsets is also removed so that the data lies between 10° and 30°. An example of the least squares solution for a single noise realization is shown in Figure 6. Repeating this experiment many times, one again finds that 2- and 3-term AVO solution estimates involve sacrifices between resolution and the accuracy.

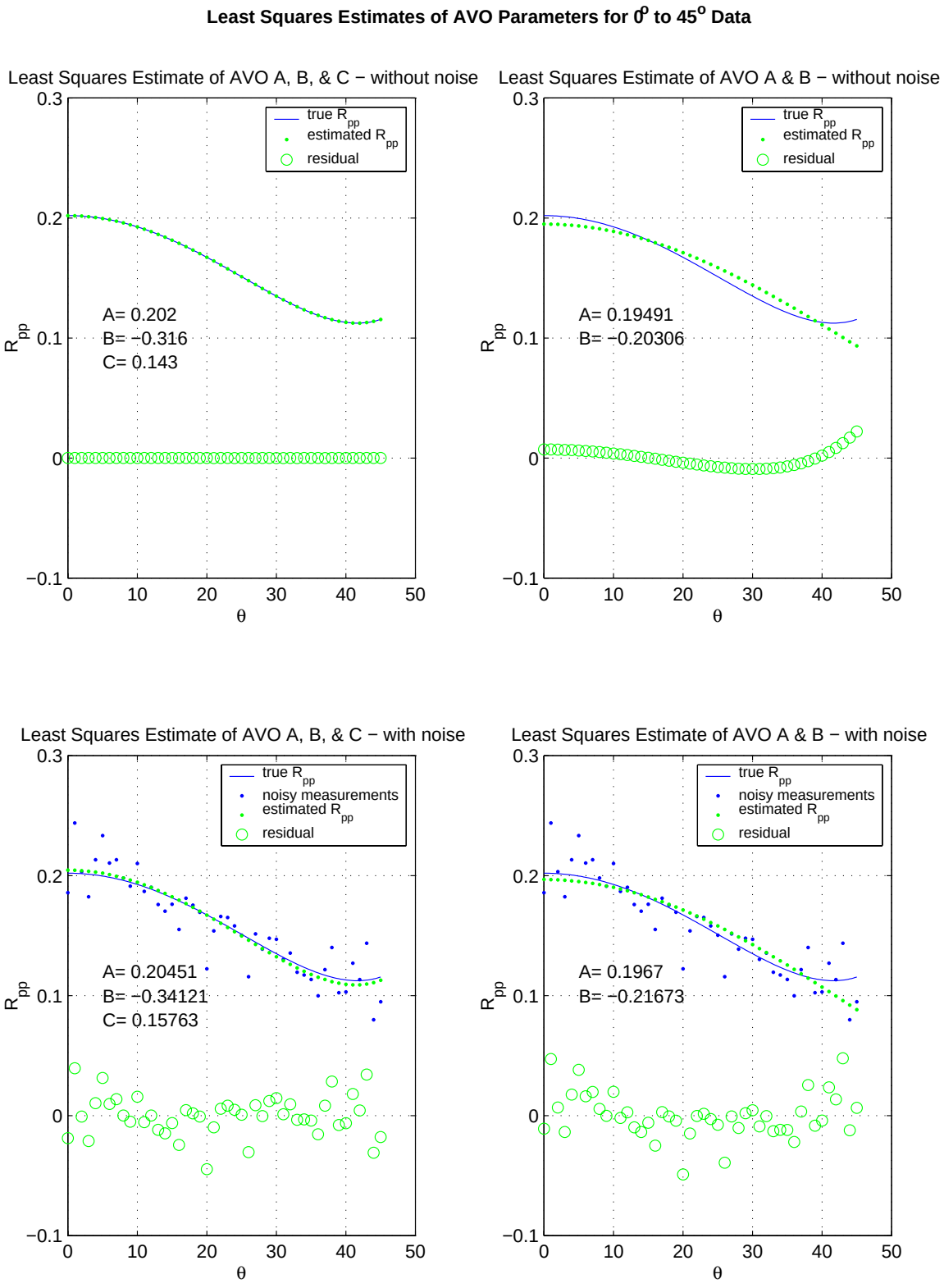

Figure 4: AVO inversion results for the two-layer model using data from 0° to 45°.

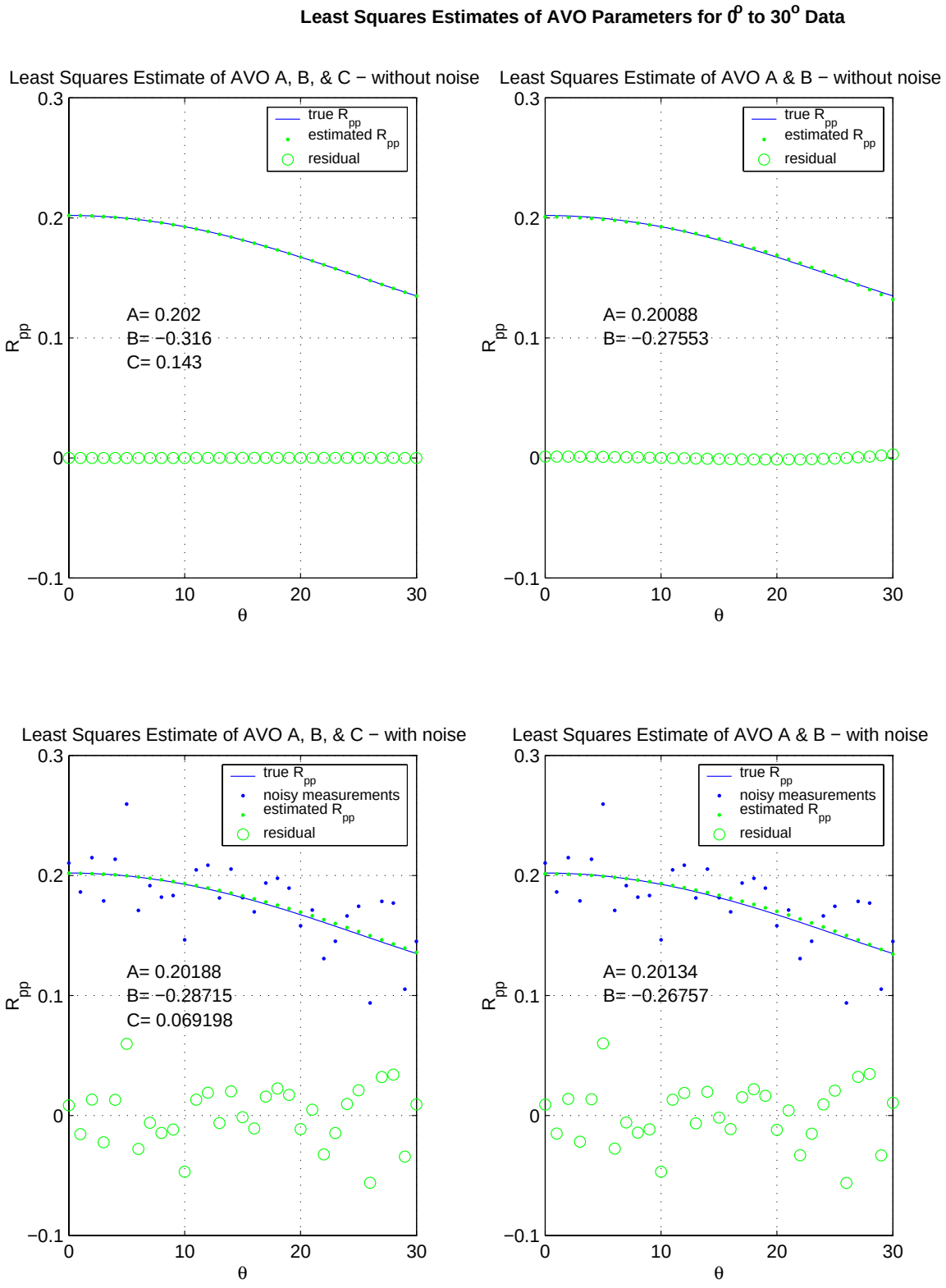

Figure 5: AVO inversion results for the two-layer model using data from 0° to 30°.

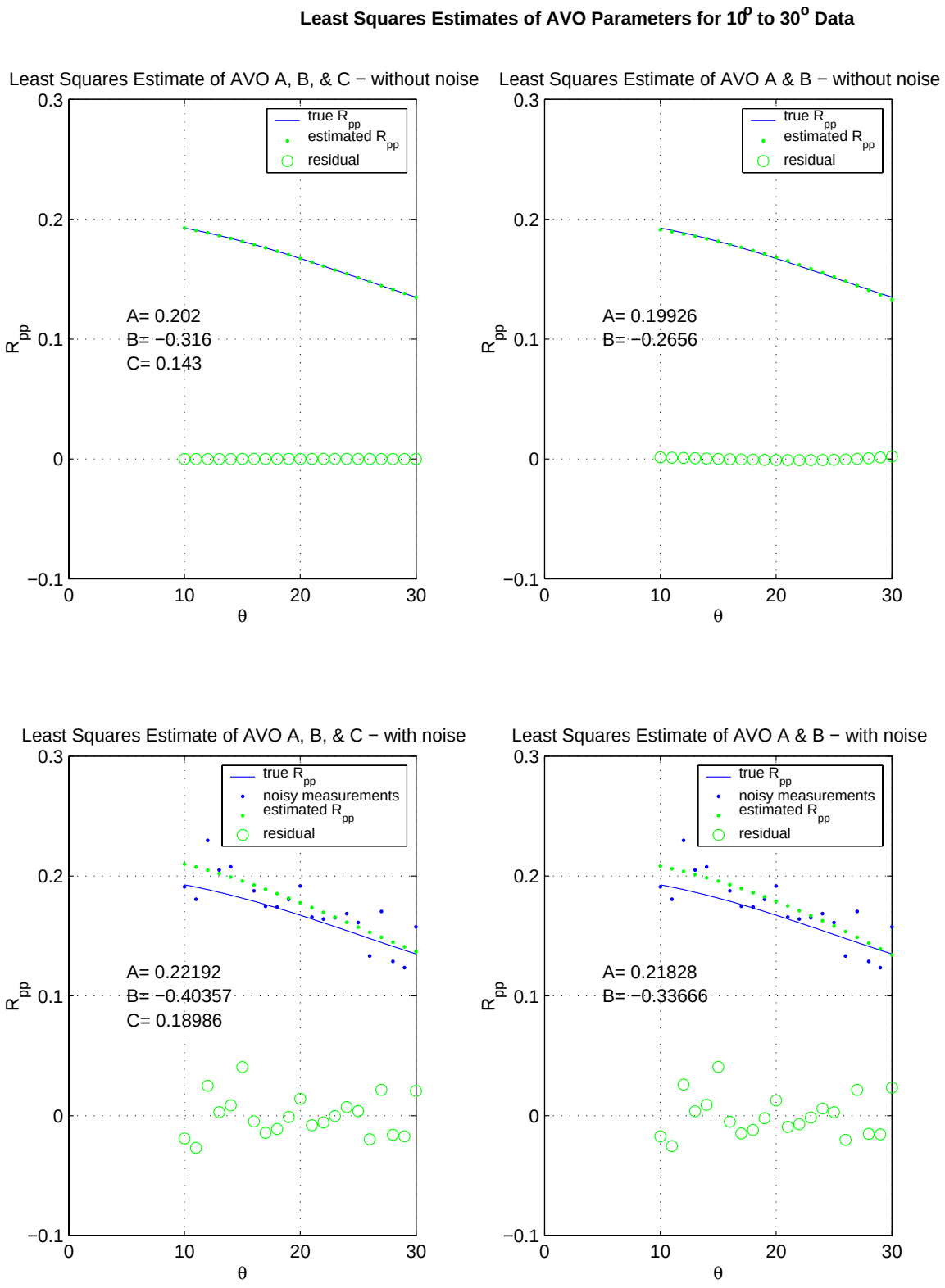

Figure 6: AVO inversion results for the two-layer model using data from 10° to 30°.

3.1.3 Discussion of Results

Based on the results of these tests over many noise realizations it is apparent that the 2-term AVO model is more appropriate in the presence of noise for the incidence angles of interest in this study. Insensitivity of the far offset 'C' term results in a 3-term solution for 'B' that is less precise than the 2-term solution. Although the far offset term contains useful information, it is commonly disregarded in AVO analysis because of the limited offsets in typical exploration surveys.

Another useful way to compare the effects of these geometries is through the use of the resolution matrix. Data resolution matrices are shown in Figure 7 for each of the previous geometry examples and for the 2- and 3-term AVO models. The 2-term model is less resolved than the 3-term model for a given geometry, but is also less sensitive to errors in the measured amplitudes at the near and far offsets. This behavior supports the argument that the 2-term model is more useful for the offset ranges considered here, especially in the presence of noise.

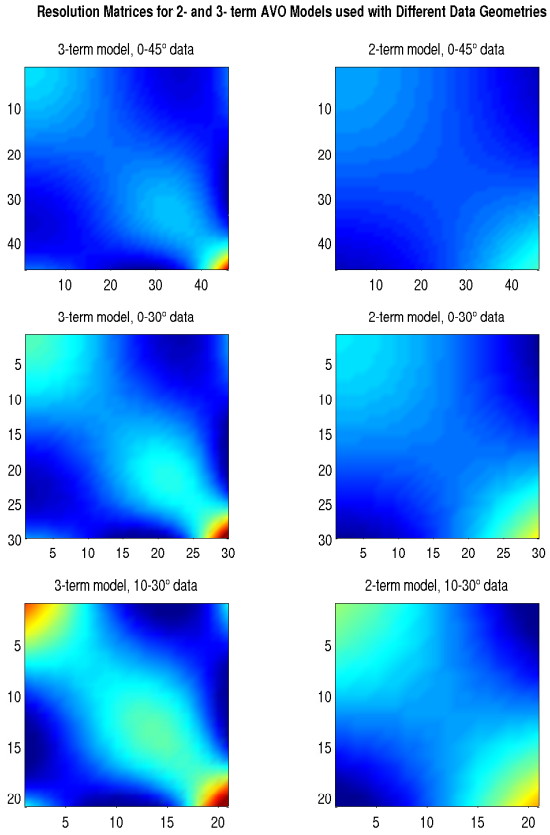

Figure 7: Resolution matrices for the least squares method using 2- and 3- term AVO models and three different cases of source-receiver geometry. N.B. Color scales are all the same and each row adds to 1.

3.2 Azimuthal AVO

3.2.1 Description of the Model and Data

A similar synthetic analysis can be preformed using azimuthal AVO, where Equation (8) is used to create the 'true' R_{PP} reflectivity model on a dense offset-azimuth grid. Synthetic data is created from this model by decimating the offset-azimuth space to represent more realistic survey geometries and random noise is added. These data are then used with Equation (12), or Equation (10) for the linearized formulation, to determine the azimuthal model parameters A, B^{iso}, B^{ani}, and φ_{sym}.

Two synthetic models are investigated using evenly distributed datasets with slightly different geometries (an example of which is shown in Figure 8) and a third model simulates the actual 3D survey geometry associated with the OBC data discussed at the end of this study. This analysis will be a good calibration tool for the results obtained when working with the actual field data. In each case, Gaussian noise with standard deviation of 0.05 is added to the 'true' R_{PP} measurements. This standard deviation corresponds to about 33% of the mean value of the noise-free data.

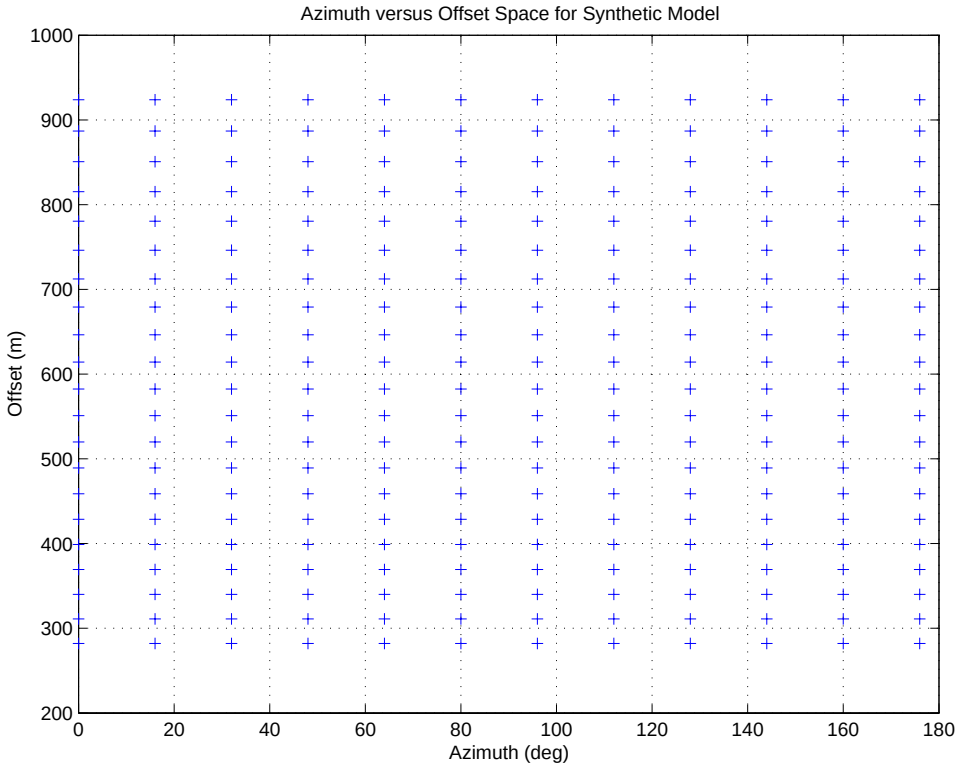

Figure 8: Azimuth-offset geometry used for synthetic AVOA analysis

For consistency with the non-azimuthal AVO analysis the same elastic model parameters are used with slight modifications for the azimuthal case. The AVO-A term is unchanged because it does not vary with azimuth. The AVO-B term is split into two parts, where 80% of the value used in the previous section is assigned to B^{iso}, and 20% to B^{ani}. An arbitrary fracture symmetry-axis orientation of 35° is used. The 'true' model parameters for the azimuthal analysis are summarized in Table 2.

A	0.202
$\mathbf{B^{iso}}$	-0.2528
$\mathbf{B^{ani}}$	-0.0632
$\mathbf{\Phi_{sym}}$	35°

Table 2: AVOA model parameters for two-layer azimuthal AVO model

The 'true' reflectivity behavior based on Equation (8) is shown in Figure 9 for a few selected azimuths. In this figure, the azimuthal behavior of the AVO gradient term is apparent. At azimuths closest to the fracture symmetry axis (35°) the greatest curvature is seen (blue and green curves) due to the contribution of the B^{ani} term. The least squares inversion aims to capture this behavior in order to uniquely and accurately determine the four model parameters.

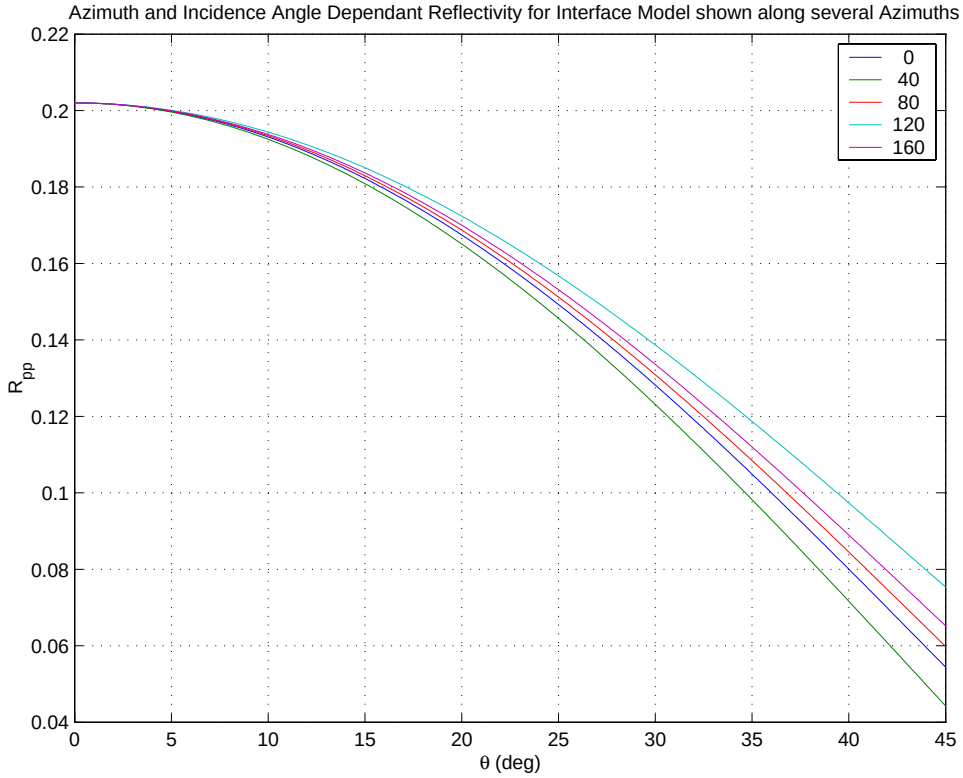

Figure 9: Synthetic AVOA model curves for several azimuths based on the parameters in Table 2.

3.2.2 Synthetic AVOA Tests

The first test of the four-term least squares inversion method is really a validation, as the input data comes from an even distribution of offsets and azimuths. The synthetic reflection amplitudes are sampled at one-degree spacing between 0° and 45° in incidence angle, and at every four degrees between 0° and 180° in azimuth. This dataset is inverted for the four AVOA model parameters using Equation (10) and the subsequent relationships between coupled linear terms in Equation (15). The inversion is repeated with 2000 realizations of the random noise, and the average results are summarized in Table 3. Note that the noise-free example has perfectly resolved the model, which should be expected because it is using a linearized form of the same model that created the data. The inversion of the noisy data has been distorted somewhat, but the AVOA parameters are resolved within reason.

Next, only the data with angles of incidence between 10° and 30°, and azimuths separated by 16° (Figure 7), are used in the same inversion process to simulate a more realistic survey geometry. Again, the average results summarized in Table 3. There is clearly a significant loss of accuracy in the inverted model when the offset-azimuth space is this parse.

Finally, the same method is used with an offset-azimuth distribution that comes from data collected during an OBC survey. This distribution is shown in Figure 10 and, though it is dense, it is not as uniformly sampled as the synthetic cases. As can be seen in Figure 3, this survey geometry has performed somewhere in-between the previous two synthetic models.

Parameter	True value	Without noise	All offsets/azimuths	Sparse offsets/azimuths	OBC geometry
A	0.202	0.202	0.2019	0.2022	0.205
B^{iso}	-0.2528	-0.2528	-0.2517	-0.2378	-0.2609
B^{ani}	-0.0632	-0.0632	-0.0645	-0.0962	-0.0621
φ_{sym}	35°	35°	34.8°	57.1°	40.1°

Table 3: Average results of azimuthal AVO inversions using noisy synthetic data for different geometries and 2000 noise realizations

3.2.3 Discussion of Results

The four-term azimuthal AVO inversion method has the fundamental ability to resolve azimuthally varying features in seismic data. The combination of survey geometry and noise content are two of the major controlling factors in the success of this approach and can clearly lead to spurious results. A more rigorous statistical analysis of various geometries and levels of noise would be a very useful tool with regards to the adequacy of AVOA analysis for a specific dataset, data preparation, and interpretation of inversion solutions. For example, an optimal scheme of offset-azimuth selection and trace stacking to suppress noise can be chosen for a specific dataset based on these statistical conclusions.

4 Field Data Analysis

4.1 Site Description

The surface-fitting approach for azimuthal AVO analysis developed in this study is applied to 3D OBC P-wave data collected over the fractured Emilio Field. The Emilio Field is situated about 25 km offshore the east cost of Italy in the central Adriatic Sea (Figure 10). This area is characterized by a NNW trending anticline formed by near E-W compression. The reservoir target is located at a depth of 2850m (~2 seconds travel time) in fractured limestone. Fractures at the reservoir level are thought to be mostly near-vertical and aligned with the direction of maximum compressive stress, which is slightly north of east.

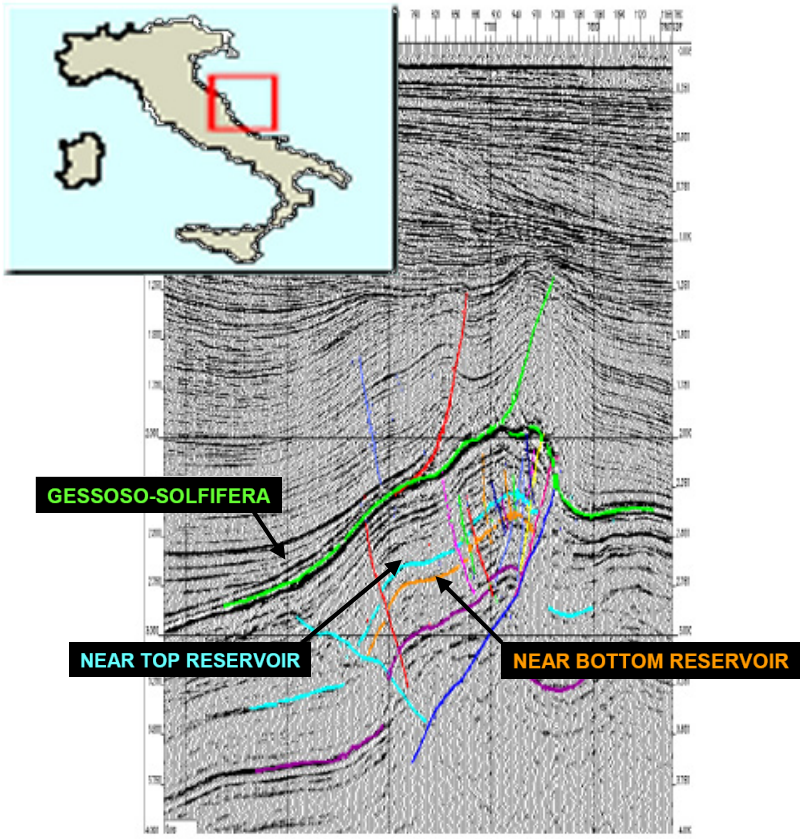

Figure 10: Location of the Emilio Field and interpreted 2D seismic section (from Gaiser *et. al.*, 2002).

Analysis of several seismic surveys over this area has attempted to characterize the anisotropic behavior in the Emilio Field due to fractures (Gaiser *et. al.*, 2002; Vetri *et. al.*, 2003). These investigations focus on shear wave birefringence and velocity analysis as anisotropy indicators, though AVO is also discussed. Results show a mostly isotropic overburden that becomes anisotropic near the reservoir level. This is corroborated with borehole and production well information including cores and televiewer logs.

4.2 Data Overview

As already discussed, one of the fundamental requirements for the application of AVOA analysis is an acquisition geometry that covers a wide range of offsets and azimuths. This OBC survey contains data over a full range of azimuths, with offsets ranging from a few hundred meters to over 4000 meters. The offset-azimuth

distribution for an 8-by-8 block of CMPs is shown in Figure 11. This pattern is a result of the acquisition method, which consists of orthogonal source and receiver lines collected over several interleaving swathes.

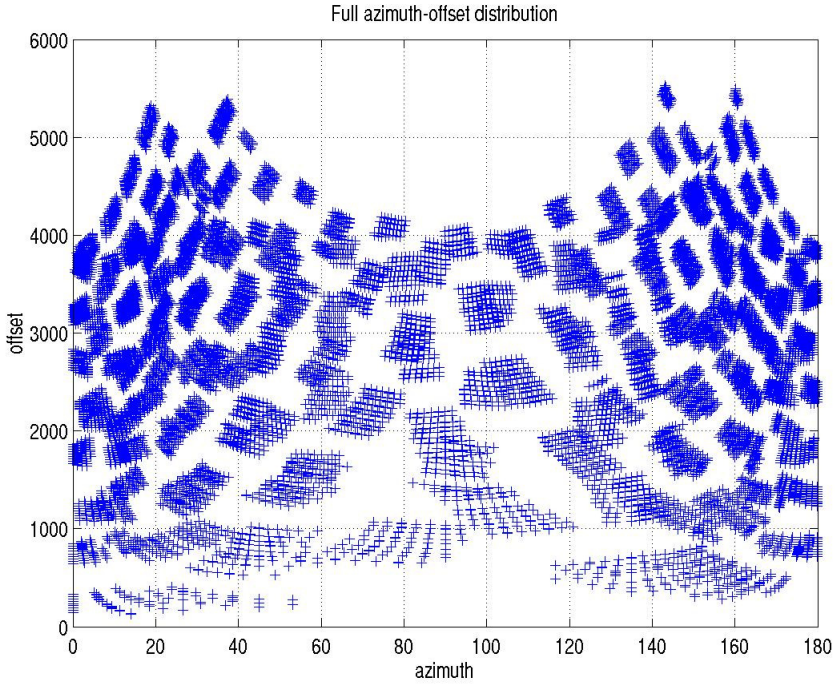

Figure 11: Offset-azimuth distribution for all traces that fall within an 8 x 8 super-CMP bin

One of the major problems commonly found with analyzing field data is noise. Because AVO analysis is performed on pre-stack data it is often difficult to obtain a good signal-to-noise ratio. Therefore, the pre-processing steps meant to enhance the signal must also be careful not to distort the natural AVO behavior. For this reason it is common to analyze more than one CMP at a time, and to stack traces with common offset-azimuth values. Although this will have the effect of blurring true amplitudes across the offset-azimuth space, it is a necessary step in overcoming the noise problem. Before performing the azimuthal AVO analysis on this super-CMP gather, several are taken to enhance the signal while regularizing the data space used in the analysis.

4.3 AVOA Analysis of Field Data

There is an obvious clustering of the traces in the block of CMPs shown in Figure 11, which is denser near zero and 180 degrees. The traces are first smoothly discretized in this offset-azimuth space so that the solution is not biased towards azimuths with more data points and to reduce the overall volume of data. The criteria for discretizing the traces are such that only one trace is accepted in any offset-azimuth bin with dimensions of 1m by 30°. The resulting dataset is shown in Figure 12 and the CMP gather corresponding to this set of traces is shown in Figure 13.

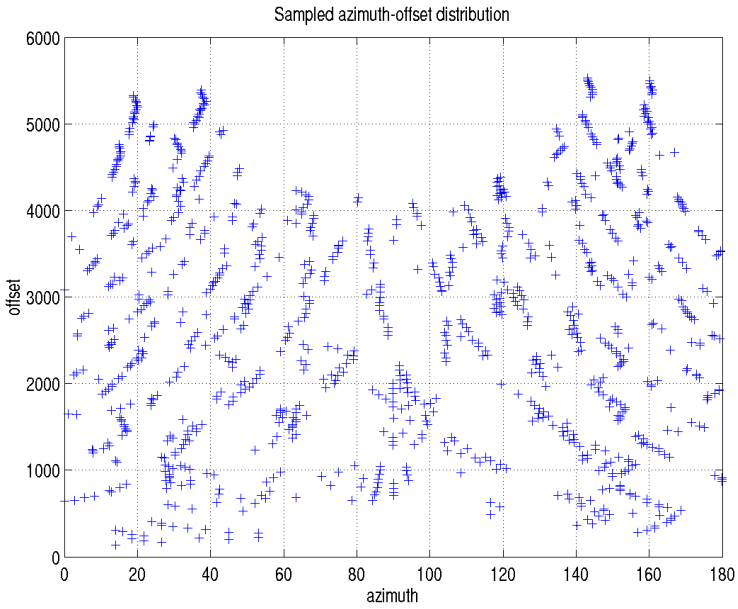

Figure 12: Regularized offset-azimuth distribution for traces in 1m by 30° bins.

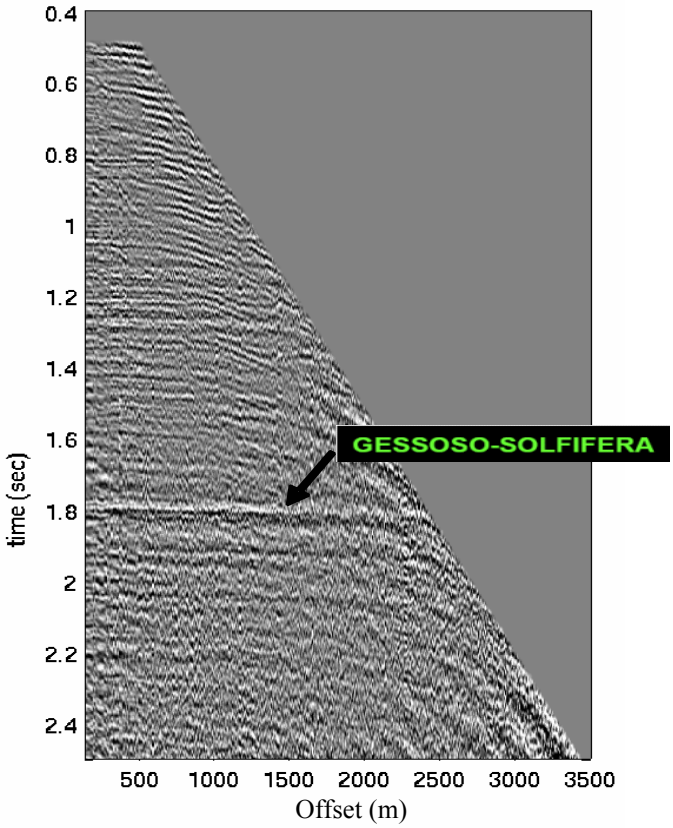

Figure 13: CMP display of the traces to be used in AVOA analysis

The traces in the super-CMP are then sorted into the common azimuth gathers shown in Figure 14. The azimuth bins are each 30 degrees wide, and are annotated with the orientation of the center of each bin. At this point, common offset stacking is applied within the azimuth gathers to enhance the signal. This involves stacking all of the traces within 100m offset groups for each azimuth gather. Besides helping to improve the signal-to-noise ratio, common offset stacking has the benefit of regularizing the offsets that are input into the inversion. Azimuth sorting is not a necessary step because the data are inverted simultaneously, but it is sometimes useful to view the data in this domain as a quality control.

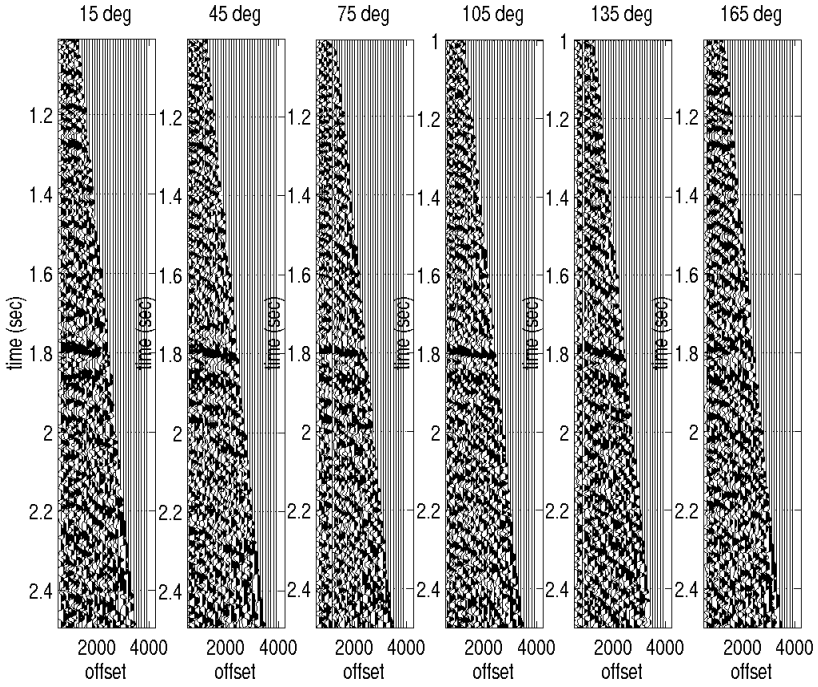

Figure 14: CMP traces sorted into 30 degree azimuth gathers and stacked on common offsets.

These azimuth gathers now contain all of the information used as input for the AVOA analysis. Using local velocity information, the time axis can be converted into approximate depths. Given the angle of incidence and source-to-receiver azimuths, the least squares method of Equation (12) is applied at incremental time steps. A 50Hz low pass filter is used to reduce the noise and windows are used to carefully select amplitude data from a reflection. The inversion produces a set of values for the four AVOA model parameters at any given time. A log-type display of the four parameters versus time is given in Figure 15.

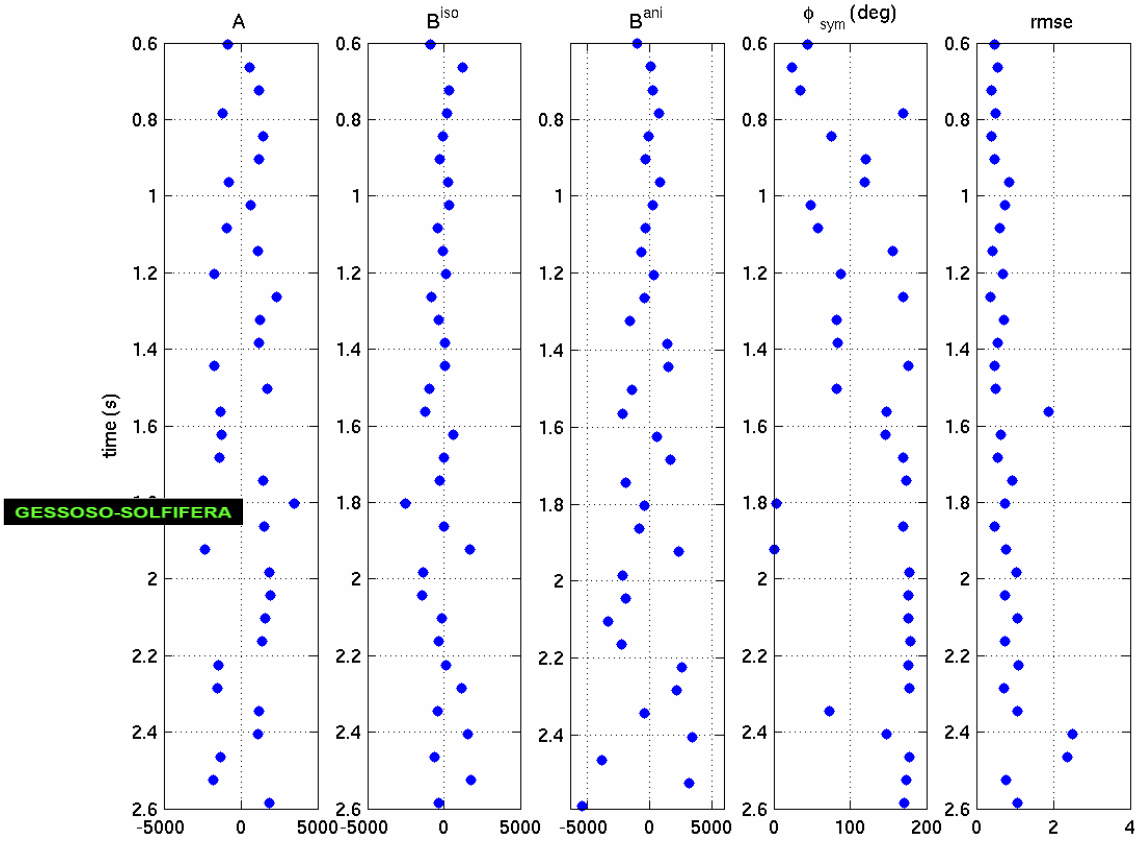

Figure 15: Azimuthal AVO parameter estimates at multiple depths for the OBC super-CMP dataset for the nonlinear inversion.

4.4 Discussion of the Field Data Inversion

Although this solution represents only a small subset of the OBC survey, there are some promising features. The relatively isotropic overburden indicated by small values of B^{ani} at early times is consistent with previous studies of this area. Increased amplitudes of B^{ani} near 1.4 seconds indicate increasing anisotropy and are well correlated with the folded structure and expected fracture zone. The most outstanding feature is the alignment of the symmetry-axis orientation near 180 degrees between 1.6 and 2.6 seconds. Because this time also correlates with increased amplitudes of B^{ani}, it is indicative of a consistent anisotropic feature within the data. These trends over long time windows suggest that the inversion is capable of resolving information within the data related to fracture orientation. The field data results have similar features as the synthetic nonlinear test in Appendix A, which also lends support to this analysis.

An investigation of individual horizons over the survey area is useful in characterizing relative spatial changes in fracture properties and can also help the interpretation of overburden effects. A preliminary result of this analysis for the Gessoso-Solifera horizon at a few selected locations in the survey is shown in Figure 16. There is a good correlation between the direction of the AVOA isotropy axis solution (blue arrows) and fast shear wave direction (red arrows showing 20° range of uncertainty) determined by Gaiser *et. al.* The magnitudes of the arrows represent the relative anisotropy at each location, but do not correlate as well as the direction. Future work will focus on analyzing this and other horizons with good spatial resolution over the entire survey area.

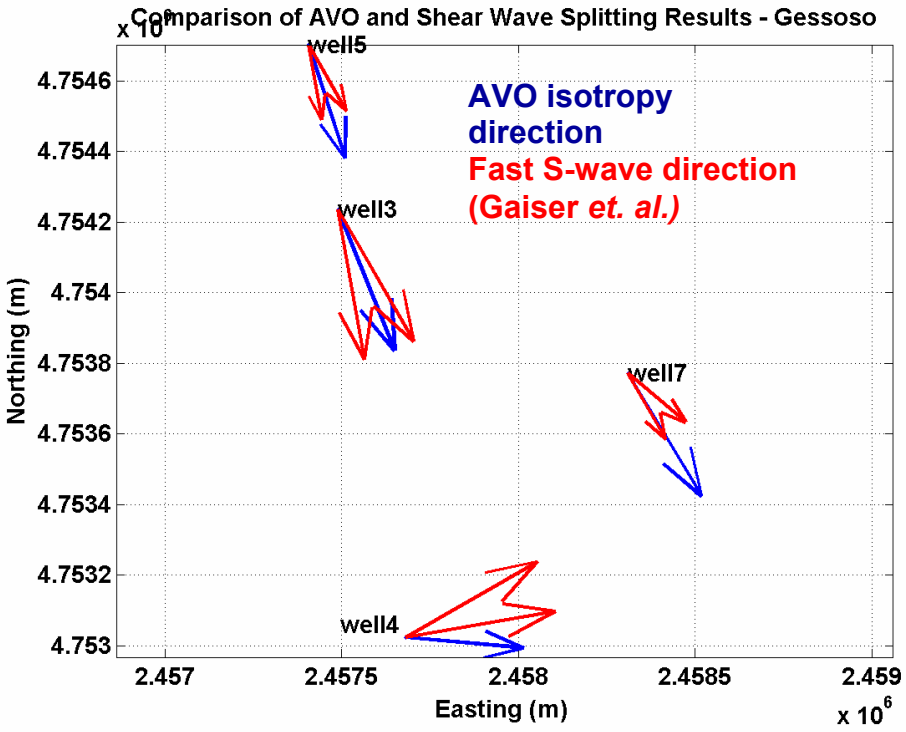

Figure 16: Comparison of the AVOA isotropy axis direction (blue) found in this study with fast S-wave direction (red) reported by Gaiser *et.al.* for the Gessoso horizon at four locations. Magnitude of the arrows represents the amount of anisotropy for each method at each location. Two fast S-wave arrows are used to show the 20° uncertainty of the direction.

5 Conclusions

This study provides a robust methodology for determining fracture information using azimuthal AVO analysis. The synthetic and field data analysis presented here supports the use of AVOA for fracture characterization, though this tool should be considered on two levels. First is the ability to detect and spatially map oriented fractured zones and describe basic features such as strike angle the extent of anisotropy. This level of detection has been successfully demonstrated in this study, though larger portions of the dataset need to be analyzed and mapped.

Understanding the behavior of this technique with different models, acquisition geometry, noise content, and pre-processing procedures is an important step. This investigation also shows that the use of an AVO model with near and mid-offset terms is sufficient for typical exploration geometries, especially in the presence of noise. A nonlinear inversion method for describing anisotropic behavior using the azimuthal AVO model derived by Rüger (1998) is supported by the analysis of several synthetic models in this study. Analyzing a full range of azimuths with this routine is more robust than the individual analysis of a few selected azimuths.

A second, more sophisticated level involves the use of AVOA information to describe the physical properties of the fractures and saturating fluid. Because of the non-uniqueness of this problem this distinction requires the incorporation of additional information. Constraints on fracture properties based on expected values of fracture density, aperture, or fluid can be used if they are known. Another option is to combine the P-wave AVOA methods discussed here with converted wave AVOA, shear wave birefringence, or other azimuthal velocity measurements, as suggested by Lynn and Cox (2003). This clearly adds significant complexity to the analysis methodology, but results in a more quantitative measure of fracture properties. Forward modeling, as discussed briefly in Appendix A, can also provide useful insights into the expected AVO behavior.

This approach was developed specifically towards describing HTI features, which may not be appropriate in all cases. A fractured reservoir may contain mostly vertical fractures, as is the case for the Emilio Field, but a certain amount of sub-vertical fractures will also be present. The addition of non-vertical fractures will result in azimuthal

anisotropy that does not fit the model of Equation (8), likely resulting in an increased data misfit. If a significant number of fractures are sub-vertical this method is inappropriate.

A second limiting factor is the overburden effect on the AVO behavior. Because of transmission through the overburden, a reflector at depth will also record the AVO imprint of shallower layers. For this reason, interpretation of AVOA results at depth should be considered carefully. Changes in the AVOA behavior with depth are representative of changes in material properties, but must be considered in the context of the overburden. Layer stripping methods have been used to remove these effects, though this is beyond the scope of this investigation.

The methods developed here are useful as a tool for the detection of fracture presence and orientation, as well as yielding information about the relative anisotropy. In particular, mapping the AVOA behavior laterally over individual horizons is useful because anomalous regions are highlighted and overburden effects can be accounted for more easily. The inclusion of forward modeling or other knowledge of fracture parameters can significantly enhance the interpretation of these results without adding significant processing complications.

6 Acknowledgements

This work was supported by the Earth Resources Laboratory Founding Members, the Department of Energy grant number DE-FC26-02NT15346, and by ENI S.p.A. AGIP.

References

Aki, K. and Richards, P.G. (1980). *Quantitative Seismology: Theory and methods.* W.H. Freeman and Co.

Castagna, J.P. (1993). AVO analysis – tutorial and review. In *Offset-Dependent Reflectivity: Theory and Practice of AVO Analysis*, pages 3-36, Tulsa. Society of Exploration Geophysicists.

Dong, W. and Davidson, M.E. (2003). Quantifying 3D acquisition adequacy for azimuthal avo analysis. *The Leading Edge*, pages 476-480.

Gaiser, J., Loinger, E., Lynn, H., and Vetri, L. (2002). Birefringence analysis at Emilio Field for fracture characterization. *First Break*, 20(8):505-514.

Hall, S.A. and Kendall, J.M. (2003). Fracture characterization at Valhall: Application of P-wave amplitude variation with offset and azimuth (AVOA) analysis to a 3D ocean-bottom data set. *Geophysics*, 68(4):1150-1160.

Lynn, H.B., Simon, K.M., Bates, C.R., and Van Dok, R. (1996). Azimuthal anisotropy in p-wave 3-D (multiazimuth) data. *The Leading Edge*, 923-928.

Lynn, H. and Cox, D., 2003, P-wave AVOA interpretation needs the input of additional information, 73rd Ann. Internat. Mtg., Soc. Expl. Geophys., Expanded Abstracts, 124-126.

Mallick, S., Craft, K.L., Meister, L.J., and Chambers, R.E. (1998). Determination of the principal directions of azimuthal anisotropy from p-wave seismic data. *Geophysics*, 63(2):692-706.

Pérez, M.A., Gibson, R.L., and Toksöz, M.N. (1999). Detection of fracture orientation using azimuthal variation of p-wave avo responses. *Geophysics*, 64(4):1253-1265.

Rüger, A. (1997). P-wave reflection coefficients for transversely isotropic models with vertical and horizontal axis of symmetry. *Geophysics*, 62(3):713-722.

Rüger, A. (1998). Variation of p-wave reflectivity with offset and azimuth in anisotropic media. *Geophysics*, 63(3):936-947.

Schoenberg, M. and Sayers, C.M. (1995). Seismic anisotropy of fractured rock. *Geophysics*, 60(1):204-211.

Shen, F., Zhu, X., and Toksöz, M.N. (2002). Effects of fractures on NMO velocities and P-wave azimuthal AVO response. *Geophysics,* 67(3):711-726.

Shuey, R.T. (1985). A simplification of the zoeppritz equations. *Geophysics*, 50(4):609-614.

Vetri, L., Loinger, E., Garner, J., Grandi, A., and Lynn, H. (2003). 3D/4C Emilio: Azimuth processing and anisotropy analysis in a fractured carbonate reservoir. *The Leading Edge*, 675-679.

Walsh, J.B. and Brace, W.F. (1964). A fracture criterion for brittle anisotropic rock. *Journal of Geophysical Research*, 69(16):3449-3456.

Xu, Y. and Li, Y. (2001). Uncertainties in azimuthal avo analysis. In *The Labours of Hercules II, AVO and AVO Reliability II*, pages 24-27. Canadian Society of Exploration Geophysicists.

Appendix A. Nonlinear AVOA analysis of 3D finite difference data using a fractured model

A nine-layer 3D model (Figure 17a) with alternating fast and slow formations given in Table 4 is constructed for the finite difference forward modeling. The middle three layers have vertical fractures oriented normal to the x-axis embedded in the background material. The fracture density (# cracks/m^3 * r^3) and aspect ratio (c/a) are 0.1 and 0.01, respectively.

	V_P (m/s)	V_S (m/s)	ρ (g/cm^3)
fast formation	4000	2352.9	2.5
slow formation	3000	1764.7	2.4

Table 4: Material properties for the synthetic model

The wide azimuth-offset distribution for this dataset is displayed in Figure 17b, and is qualitatively similar to that used for the Emilio Field analysis. CMP data created from the finite difference results with this model are shown in Figure 17c after NMO, spherical divergence correction, and mute.

For each reflection in Figure 17a the data are inverted for the four AVOA parameters using the non-linear inversion routine discussed above. Results of the inversion are shown in Figure 17d-e. Figure 17d shows model predictions for the azimuthal reflection amplitudes (left) and azimuthal variation in the AVO gradient (right) for a reflection exhibiting anisotropic behavior due to the fractures. Figure 17e displays all four AVOA parameters at each reflector. General trends expected from the alternating lithology and fractured layers can be seen, though distortion due to the overburden is evident in the deeper layers.

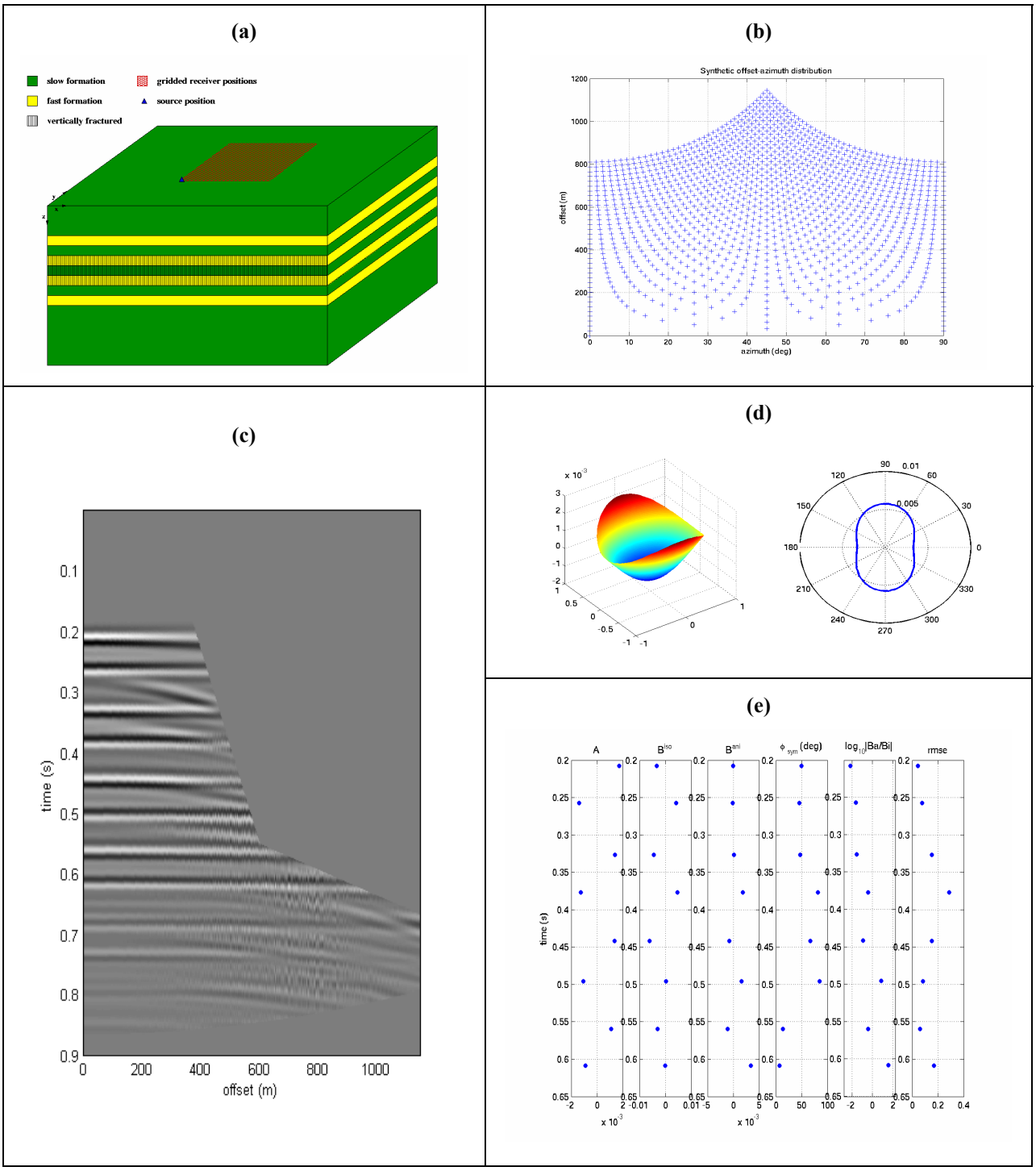

Figure 17: Synthetic model and AVOA results. (a) Nine-layer synthetic model with properties given in Table 4. (b) Azimuth-offset distribution for the synthetic model. (c) Finite difference results for synthetic model after NMO, spherical divergence correction, and mute. (d) Example of inverted AVOA behavior for an interface that exhibits anisotropy. Left side shows amplitude behavior as a function of offset and azimuth, right side shows the azimuthal variation of the AVO gradient, correctly oriented near zero degrees. (e) AVOA inversion results for all eight reflections showing the effect of the alternating layers and fractures, though overburden effects are present.